Journal of Advanced Ceramics
2023, **12**(5): 916–929
https://doi.org/10.26599/JAC.2023.9220727
ISSN 2226-4108
CN 10-1154/TQ

Research Article

Reduced He ion irradiation damage in ZrC-based high-entropy ceramics

Xiao-Ting Xin[a,c,†], Weichao Bao[a,†,*], Xin-Gang Wang[a,*], Xiao-Jie Guo[a,c], Ying Lu[d], Chenxi Zhu[a], Ji-Xuan Liu[b], Qiang Li[a], Fangfang Xu[a,*], Guo-Jun Zhang[b]

[a]*State Key Laboratory of High Performance Ceramics and Superfine Microstructure, Shanghai Institute of Ceramics, Shanghai 200050, China*
[b]*State Key Laboratory for Modification of Chemical Fibers and Polymer Materials, Institute of Functional Materials, Donghua University, Shanghai 201620, China*
[c]*University of Chinese Academy of Sciences, Beijing 100049, China*
[d]*School of Engineering, Westlake University, Hangzhou 310024, China*

Received: November 17, 2022; Revised: December 30, 2022; Accepted: January 30, 2023

Abstract: Excellent irradiation resistance is the basic property of nuclear materials to keep nuclear safety. The high-entropy design has great potential to improve the irradiation resistance of the nuclear materials, which has been proven in alloys. However, whether or not high entropy can also improve the irradiation resistance of ceramics, especially the mechanism therein still needs to be uncovered. In this work, the irradiation and helium (He) behaviors of zirconium carbide (ZrC)-based high-entropy ceramics (HECs), i.e., $(Zr_{0.2}Ti_{0.2}Nb_{0.2}Ta_{0.2}W_{0.2})C$, were investigated and compared with those of ZrC under 540 keV He ion irradiation with a dose of 1×10^{17} cm^{-2} at room temperature and subsequent annealing. Both ZrC and $(Zr_{0.2}Ti_{0.2}Nb_{0.2}Ta_{0.2}W_{0.2})C$ maintain lattice integrity after irradiation, while the irradiation-induced lattice expansion is smaller in $(Zr_{0.2}Ti_{0.2}Nb_{0.2}Ta_{0.2}W_{0.2})C$ (0.78%) with highly thermodynamic stability than that in ZrC (0.91%). After annealing at 800 ℃, ZrC exhibits the residual 0.20% lattice expansion, while $(Zr_{0.2}Ti_{0.2}Nb_{0.2}Ta_{0.2}W_{0.2})C$ shows only 0.10%. Full recovery of the lattice parameter (a) is achieved for both ceramics after annealing at 1500 ℃. In addition, the high entropy in the meantime brings about the favorable structural evolution phenomena including smaller He bubbles that are evenly distributed without abnormal coarsening or aggregation, segregation, and shorter and sparser dislocation. The excellent irradiation resistance is related to the high-entropy-induced phase stability, sluggish diffusion of defects, and stress dispersion along with the production of vacancies by valence compensation. The present study indicates a high potential of high-entropy carbides in irradiation resistance applications.

Keywords: high-entropy carbides; zirconium carbide (ZrC); irradiation damage; dislocations; helium (He) bubbles

† Xiao-Ting Xin and Weichao Bao contributed equally to this work.

* Corresponding authors.
E-mail: W. Bao, baoweichao@mail.sic.ac.cn;
X.-G. Wang, xgwang@mail.sic.ac.cn;
F. Xu, ffxu@mail.sic.ac.cn

1 Introduction

With the research and development of advanced nuclear power systems, it is worthwhile devoting much effort to developing novel nuclear materials to adapt to extreme conditions, such as high temperatures, severe corrosion, and strong irradiation [1–3]. Transition metal carbide ceramics, such as zirconium carbide (ZrC) [4–6], TiC [5,7], TaC [5,8], NbC [4,9,10], and WC [5,11], are proposed to be candidates for the advanced nuclear power systems, due to their high melting points (Table 1), good high-temperature mechanical properties, and excellent irradiation resistance. Among these carbides, ZrC is considered to be the most promising candidate for structural components in tristructural isotropic (TRISO) coated nuclear fuel [12] and high-temperature gas-cooled reactor (HTGCR) (the maximum helium (He) ion concentration of ~3–40 atomic part per million (appm)) [13] owing to a much smaller neutron absorption cross-section of Zr than those of other transition metal elements, as can be seen in Table 1.

He ions can be generated in the fission and fusion reactor, which not only displace atoms of materials through cascade collision but also aggregate to form He bubbles, leading to degradation and even failure of the nuclear materials [18,19]. Thus, how to suppress the growth of the He bubbles in the nuclear materials is of pivotal interest for the safety of advanced nuclear systems.

The high-entropy concept provides an opportunity for the design of irradiation resistance materials from nano and atomic scales. Reference [20] shows that single-phase solid solution high-entropy alloys (HEAs) maintain relatively high phase stability under very high irradiation doses at room temperature [20]. Damage accumulation, swelling, segregation, He bubbles, and void formation are found to be considerably suppressed in Ni-based single-phase concentrated solid solution alloys [21–27]. Molecular dynamics simulations indicate a variety of kinetics responsible for the enhanced irradiation resistance of the HEAs. They include a short-range three-dimensional mode of defect cluster motion [28], enhanced thermal spike and decreased thermal conductivity with low binding energy (BE) of interstitial loops [22], increased self-interstitial atom migration energy, and absence of a subcascade [29].

Different from the metallic bond-based HEAs, high-entropy ceramics (HECs) usually possess a mixture of covalent, ionic, and metallic bonds [30]. The amorphization resistance of non-metallic materials under irradiation depends on the competition between short-range covalent and long-range ionic forces. As-damaged ionic structures have a larger chance to re-establish their coherence with the lattice by electrostatic charge [31]. In addition, the charge compensation is typical in the HECs when the elements with different valence states are mixed. The vacancies can be formed to maintain valence balance [32], which can restrain the lattice expansion during irradiation [18,33]. Up to the present, there are very few related studies on the irradiation behavior of the HECs, particularly high-entropy carbide ceramics. Wang *et al*. [34,35] irradiated high-entropy $(Hf_{0.2}Zr_{0.2}Ta_{0.2}Nb_{0.2}Ti_{0.2})C$ by 120 keV He ions at room temperature and found that the He bubbles exhibit a uniform small size (1 nm) and are evenly distributed at an irradiated layer. They also investigated the irradiation behavior of four-membered carbide solid solution $(Zr_{0.25}Ta_{0.25}Nb_{0.25}Ti_{0.25})C$ by 3 MeV Zr ions at different temperatures and found that the ceramics maintain high phase stability without void formation or irradiation-induced segregation. Zhu *et al*. [36] observed a similar phenomenaon in irradiated $(WTiVNbTa)C_5$ with 1 MeV C ions at room temperature and 650 ℃. However, so far, it still lacks a clear understanding of whether and how significantly the high-entropy carbides could demonstrate better irradiation resistance over the single carbide.

Table 1 Melting points and bond dissociation energy of five single carbides; neutron absorption cross-sections and atomic covalent radii of five transition metal elements

Carbide	TiC	ZrC	NbC	TaC	WC	Ref.
Melting point (℃)	3067	3420	3600	3950	2870	[14]
Bond dissociation energy (eV)	4.09	6.91	5.39	8.73	5.26	[15,16]
Transition metal element	Ti	Zr	Nb	Ta	W	Ref.
Neutron absorption cross-section (b)	6.1	0.2	1.2	20.5	18.4	[8,17]
Atomic covalent radius (pm)	160	175	164	170	162	—

In this work, the 540 keV He ion irradiation with a dose of 1×10^{17} cm^{-2} was performed at room temperature on both ZrC and single-phase $(Zr_{0.2}Ti_{0.2}Nb_{0.2}Ta_{0.2}W_{0.2})C$ high-entropy carbide ceramics. Irradiation-induced structural evolution and He retention behaviors after annealing at different temperatures were examined in depth by grazing incident X-ray diffraction (GIXRD), X-ray photoelectron spectroscopy (XPS), scanning electron microscopy, transmission electron microscopy, energy dispersive spectroscopy (EDS), and theoretical investigations of irradiation-induced atomic displacement, distribution of He ions, and strain fields. The high entropy improving the irradiation resistance over the single carbide is confirmed, and the enhancement mechanism is discussed.

2 Materials and methods

2. 1 Synthesis of ceramics

Microcrystalline $(Zr_{0.2}Ti_{0.2}Nb_{0.2}Ta_{0.2}W_{0.2})C$ and ZrC ceramics were prepared by hot pressing of self-synthesized carbide powders, which were obtained by carbothermal reduction of commercial ZrO_2 (99.95%, ~0.2 μm), TiO_2 (99.99%, ~0.1 μm), Nb_2O_5 (99.9%, ~3 μm), Ta_2O_5 (99.9%, ~1.5 μm), WO_3 (99.9%, ~74 μm), and graphite (99.9%, ~2 μm). Firstly, commercial oxide powders in the proportion of the equimolar ratio of transition metals ($n_{ZrO_2} : n_{TiO_2} : n_{Nb_2O_5} : n_{Ta_2O_5} : n_{WO_3}$ = 2 : 2 : 1 : 1 : 2) were mixed with a corresponding proportion of graphite in ethanol, followed by ball milling using ZrO_2 ball media for 24 h. After removing the ethanol through rotary evaporation, the powder mixture was molded and heated to 1600 ℃ for 1 h under vacuum. Then the synthesized carbide powders were sieved with a 200 mesh screen, and then placed in a graphite mold. Finally, the carbide powder mixture was hot pressed for 1 h under flowing argon (purity > 99.9%) with a uniaxial pressure of 30 MPa. The hot pressing temperature of $(Zr_{0.2}Ti_{0.2}Nb_{0.2}Ta_{0.2}W_{0.2})C$ was 2100 ℃, while that of ZrC was 2000 ℃. The relative densities of the as-manufactured ZrC and $(Zr_{0.2}Ti_{0.2}Nb_{0.2}Ta_{0.2}W_{0.2})C$ are both higher than 94%.

2. 2 He ion irradiation

The as-synthesized ceramics of both ZrC and $(Zr_{0.2}Ti_{0.2}Nb_{0.2}Ta_{0.2}W_{0.2})C$ were polished, and then irradiated by a 540 keV He^{2+} ion beam at room temperature in a 320 kV platform for the multi-disciplinary research with highly charged ions at Institute of Modern Physics, Chinese Academy of Sciences. The chamber was pumped to a pressure of < 10^{-4} Pa before irradiation, and the vacuum was maintained during irradiation. The surfaces of the irradiated samples were set perpendicular to the direction of the He^{2+} ion beam, and then they were irradiated with an ion fluence (F) of 1×10^{17} cm^{-2} at room temperature. The as-irradiated ceramics were then cut into small pieces by wire electrical discharge machining, and some of them were annealed at 800 and 1500 ℃ for 2 h under flowing argon (purity > 99.9%) in a furnace (NM8 20-1Z2-21SP, NEMS Co., Ltd., Japan).

2. 3 Characterization

Phase compositions of the as-hot-pressed ceramics were examined by an X-ray diffractometer (D8 DISCOVER DAVINCI, Bruker AXS GmbH, Germany) using Cu Kα radiation. To investigate the phase structural evolution along the depth, all specimens were then characterized by a grazing incident X-ray diffractometer (D/max 2550V, Rigaku, Japan) with Cu Kα radiation. The diffractometer was operated at grazing incidence angles (θ) of 3.0° and 4.5° for ZrC and $(Zr_{0.2}Ti_{0.2}Nb_{0.2}Ta_{0.2}W_{0.2})C$, respectively, with a scanning speed of 2° min^{-1}. XPS analysis was carried out on an X-ray photoelectron spectroscope (K-Alpha, Thermo Scientific, USA) with a Al Kα source ($h\nu$ = 1486.6 eV, where h is the Planck constant, and ν is the phonon frequency). Microstructures were investigated by a scanning electron microscope (SEM; TM3000, Hitachi, Japan) and a 200 kV transmission electron microscope (TEM; Tecnai G2 F20, FEI, USA). A spherical aberration-corrected TEM (AC-TEM; HF5000, Hitachi, Japan) equipped with a dual-energy dispersive spectrometer (X-Max 100 LTE, Oxford, UK) was used to examine the microstructures of the samples on the nano and atomic scales. Cross-section TEM samples were prepared by a focused ion beam (FIB; Nova 600 Nanolab, FEI, USA) facility.

2. 4 Calculation

Displacement damage and concentration distributions of the He ions after 540 keV He ion irradiation with a dose of 1×10^{17} cm^{-2} were calculated by the Stopping and Range of Ions in Matter (SRIM) [37]. The input parameters for SRIM simulations are summarized in Table 2.

Table 2 Input parameters for SRIM simulations

Input parameter	Value
Calculation type	Kinchin–Pease
Ion specie	He
Ion energy (keV)	540
Target width (nm)	2000
Target density (g/cm^3)	6.64 and 9.92 for ZrC and $(Zr_{0.2}Ti_{0.2}Nb_{0.2}Ta_{0.2}W_{0.2})C$, respectively
Target composition	ZrC and $(Zr_{0.2}Ti_{0.2}Nb_{0.2}Ta_{0.2}W_{0.2})C$
Number of ions	10,000
Displacement energy E_d (eV)	C 25 [38] and Zr 35 [38] C 25 [38], Zr 35 [38], Ti 23 [39,40], Nb 24 [41], Ta 32 [42], and W 24 [43]

Theoretical densities of ZrC and $(Zr_{0.2}Ti_{0.2}Nb_{0.2}Ta_{0.2}W_{0.2})C$ were calculated based on their lattice volumes, as tested by XRD patterns (Fig. 1(c)).

The strain fields were calculated via a finite element method using the COMSOL Multiphysics software (version 5.3b, COMSOL, Sweden) in the solid mechanics package. The computational domain was refined to 1856 triangular elements with two-dimensional (2D) geometry. The simulations aimed to obtain the strain distribution upon different residual stress inside bulk materials. The vertical component compressive stress was set as 3 GPa, and the residual stress was set as 1 GPa inside the bulk.

3 Results and discussion

3.1 Structures and microstructures of as-hot-pressed $(Zr_{0.2}Ti_{0.2}Nb_{0.2}Ta_{0.2}W_{0.2})C$ and ZrC

Densified $(Zr_{0.2}Ti_{0.2}Nb_{0.2}Ta_{0.2}W_{0.2})C$ and ZrC ceramics were successfully prepared by hot pressing at 2100 and 2000 ℃, respectively. Their typical microstructures in the polycrystalline are shown in backscattered electron (BSE) images (Figs. 1(a) and 1(b)). Each crystallite is clearly distinguished by different contrast of the grains on the polished surface. The contrast of the grains is determined by crystal orientation according to the lattice channeling effect. The higher the yields of the BSEs, the brighter the crystal grains appear in the BSE images. The areas with the darkest contrast are carbon residue (marked by the yellow circles in Figs. 1(a) and 1(b)), and the areas with the darkest contrast and white edges are voids (marked by the red circles in

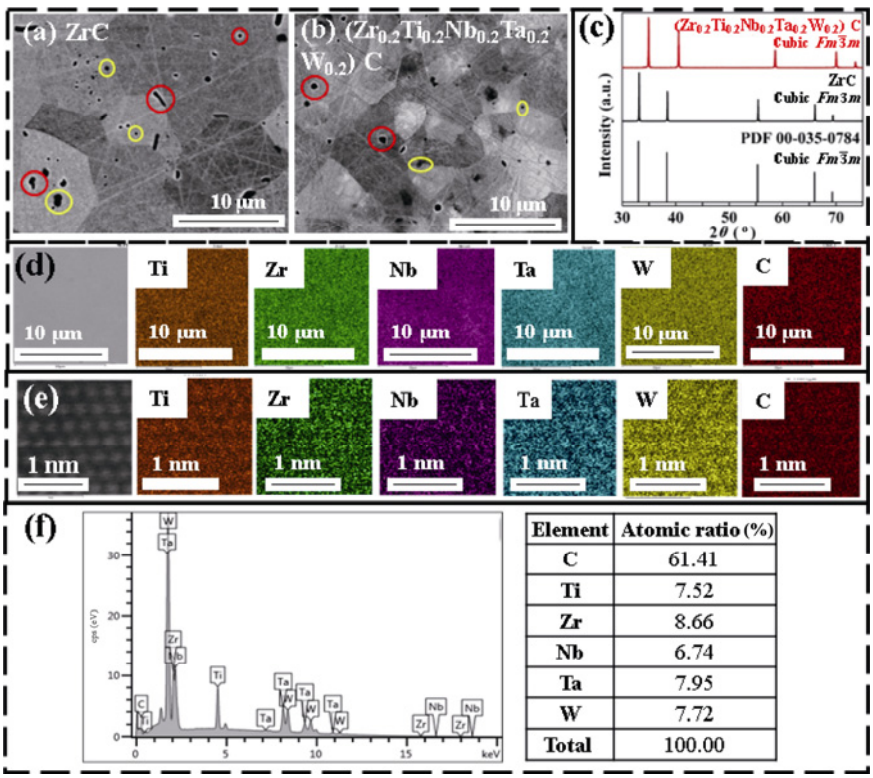

Element	Atomic ratio (%)
C	61.41
Ti	7.52
Zr	8.66
Nb	6.74
Ta	7.95
W	7.72
Total	100.00

Fig. 1 BSE images of as-manufactured polycrystalline (a) ZrC and (b) $(Zr_{0.2}Ti_{0.2}Nb_{0.2}Ta_{0.2}W_{0.2})C$. (c) XRD patterns of hot pressed samples $(Zr_{0.2}Ti_{0.2}Nb_{0.2}Ta_{0.2}W_{0.2})C$ and ZrC. (d) Secondary electron image and corresponding EDS mappings of $(Zr_{0.2}Ti_{0.2}Nb_{0.2}Ta_{0.2}W_{0.2})C$. (e) Atomic high-angle annular dark-field (HAADF) image and corresponding EDS mappings of as-hot-pressed $(Zr_{0.2}Ti_{0.2}Nb_{0.2}Ta_{0.2}W_{0.2})C$. (f) EDS spectra and measured atomic ratios of as-hot-pressed $(Zr_{0.2}Ti_{0.2}Nb_{0.2}Ta_{0.2}W_{0.2})C$.

Figs. 1(a) and 1(b)), which are usually present in most of the ceramics. Regardless of the voids, the mean grain sizes are measured to be 4.00±1.53 and 9.94± 5.15 μm for $(Zr_{0.2}Ti_{0.2}Nb_{0.2}Ta_{0.2}W_{0.2})C$ and ZrC, respectively. According to Ref. [44], the grains in the micron size range do not show an observable discrepancy in irradiation damage. Therefore, the factor of difference in the grain size between $(Zr_{0.2}Ti_{0.2}Nb_{0.2}Ta_{0.2}W_{0.2})C$ and ZrC could be excluded in discussing the mechanism of the irradiation behavior in the present study. The XRD patterns (Fig. 1(c)) indicate single-phase face-centered cubic (FCC) structures for both ceramics, where all diffraction peaks are sharp without splitting. Characteristic peaks of $(Zr_{0.2}Ti_{0.2}Nb_{0.2}Ta_{0.2}W_{0.2})C$ are located at larger angles and hence the lattice parameter (a) is smaller than those of ZrC, which are due to the larger ionic radius of Zr than those of other transition elements. The EDS elemental mappings on the micro and atomic scales (Figs. 1(d) and 1(e)) show that the transition metals are distributed homogeneously in $(Zr_{0.2}Ti_{0.2}Nb_{0.2}Ta_{0.2}W_{0.2})C$, and the measured average composition of Ti : Zr : Nb : Ta : W = 1 : 1.15 : 0.90 : 1.06 : 1.03 is close to the equimolar ratio (Fig. 1(f)).

3. 2 Structural and microstructural evolution of $(Zr_{0.2}Ti_{0.2}Nb_{0.2}Ta_{0.2}W_{0.2})C$ and ZrC under He ion irradiation

The as-sintered ZrC and $(Zr_{0.2}Ti_{0.2}Nb_{0.2}Ta_{0.2}W_{0.2})C$ ceramics were irradiated by 540 keV He ions with a high dose of 1×10^{17} cm^{-2} at room temperature. After irradiation, the GIXRD was conducted to examine the structural evolution at the irradiation damage layer close to the sample surface for both ceramics. Taking the θ = 3.0° and 4.5° for ZrC and $(Zr_{0.2}Ti_{0.2}Nb_{0.2}Ta_{0.2}W_{0.2})C$, respectively, the corresponding penetration depths of X-rays are about ~1.50 and ~1.23 μm, respectively, as estimated according to Beer–Lambert law [45]. The diffraction peaks of both ZrC and $(Zr_{0.2}Ti_{0.2}Nb_{0.2}Ta_{0.2}W_{0.2})C$ keep sharp (Fig. 2(a)), indicating the maintenance of single-phase crystallinity of the FCC structure during He irradiation. The peak splitting phenomenon of irradiated ZrC is because the incident depth of 1.50 μm exceeds the damage depth of irradiated ZrC at θ = 3.0°, which contains part of the structural information from the unirradiated region. In addition, it can be found that all diffraction peaks shift to lower 2θ after He irradiation, suggesting irradiation-induced swelling of the crystal lattices in both ZrC and $(Zr_{0.2}Ti_{0.2}Nb_{0.2}Ta_{0.2}W_{0.2})C$, a common phenomenon in the irradiation process. However, such lattice expansion is smaller in $(Zr_{0.2}Ti_{0.2}Nb_{0.2}Ta_{0.2}W_{0.2})C$ (~0.78%) than that in ZrC (~0.91%) after measuring a and its comparative variation ($\Delta a/a$), as shown in Figs. 2(b) and 2(c), respectively.

Cross-sectional microstructures of the as-irradiated ZrC and $(Zr_{0.2}Ti_{0.2}Nb_{0.2}Ta_{0.2}W_{0.2})C$ are displayed in Figs. 3(b) and 3(f), respectively. There is a clear interface separating damaged and undamaged areas (IDUA) by noting sharp change in imaging contrast. The interface is parallel to and locates at a certain depth beneath the flat sample surface. No voids or dislocations could be observed in both irradiated ceramics. The measured depth of the IDUA is ~1.00 μm in ZrC ceramics and ~1.18 μm in $(Zr_{0.2}Ti_{0.2}Nb_{0.2}Ta_{0.2}W_{0.2})C$ ceramics, which basically matches the SRIM calculation (Figs. 3(a) and 3(e), respectively). However, the calculation predicts a smaller irradiation depth in $(Zr_{0.2}Ti_{0.2}Nb_{0.2}Ta_{0.2}W_{0.2})C$ (~1.16 μm) than that in ZrC (~1.34 μm), as estimated by the consideration of the lower longitudinal depth of damage in ceramics of higher densities [37], i.e., in this case, 9.92 g/cm^3 of $(Zr_{0.2}Ti_{0.2}Nb_{0.2}Ta_{0.2}W_{0.2})C$ is higher than 6.64 g/cm^3 of ZrC. Such difference between the theoretical calculations and the experimental observations could be attributed to the ignorance of thermal effects and crystal structures in the theoretical calculations. Identical to the sharp diffraction peaks in the GIXRD patterns, selected area electron diffraction (SAED) patterns of the damaged area (Figs. 4(b) and 4(f)) also show strong and round diffraction spots without the appearance of any extra reflections, again confirming the sustained lattice integrity after He irradiation in both carbide ceramics. However, TEM bright-field (BF) images (Figs. 3(b) and 3(f)) show the different diffraction contrast. Tiny mottled contrast is observed in the whole irradiated area of ZrC from the surface to the IDUA, while this could only be detectable within the narrow depth near the IDUA in irradiated $(Zr_{0.2}Ti_{0.2}Nb_{0.2}Ta_{0.2}W_{0.2})C$, and the dark dots have the much smaller sizes (Figs. 4(a) and 4(e)). The mottled contrast refers to the clusters of point defects. The aggregation of irradiation-induced point defects seems to take place only at the region with peaked He ion residence (Fig. 3(e)) in $(Zr_{0.2}Ti_{0.2}Nb_{0.2}Ta_{0.2}W_{0.2})C$, while it becomes difficult in the area near the sample surface, and instead a large lattice strain is produced, as indicated by dense strain streaks (Fig. 3(f)). Actually, all of the five solution metal ions keep evenly distributed in as-irradiated $(Zr_{0.2}Ti_{0.2}Nb_{0.2}Ta_{0.2}W_{0.2})C$, as evidenced by the EDS examination (Fig. 5(b)). Thus, albeit a little bit larger irradiation depth in $(Zr_{0.2}Ti_{0.2}Nb_{0.2}Ta_{0.2}W_{0.2})C$,

i.e., the larger area suffering from irradiation damage, structural changes and sizes of defects are much smaller, and hence lower severity of damages than those in the ZrC ceramics can be obtained.

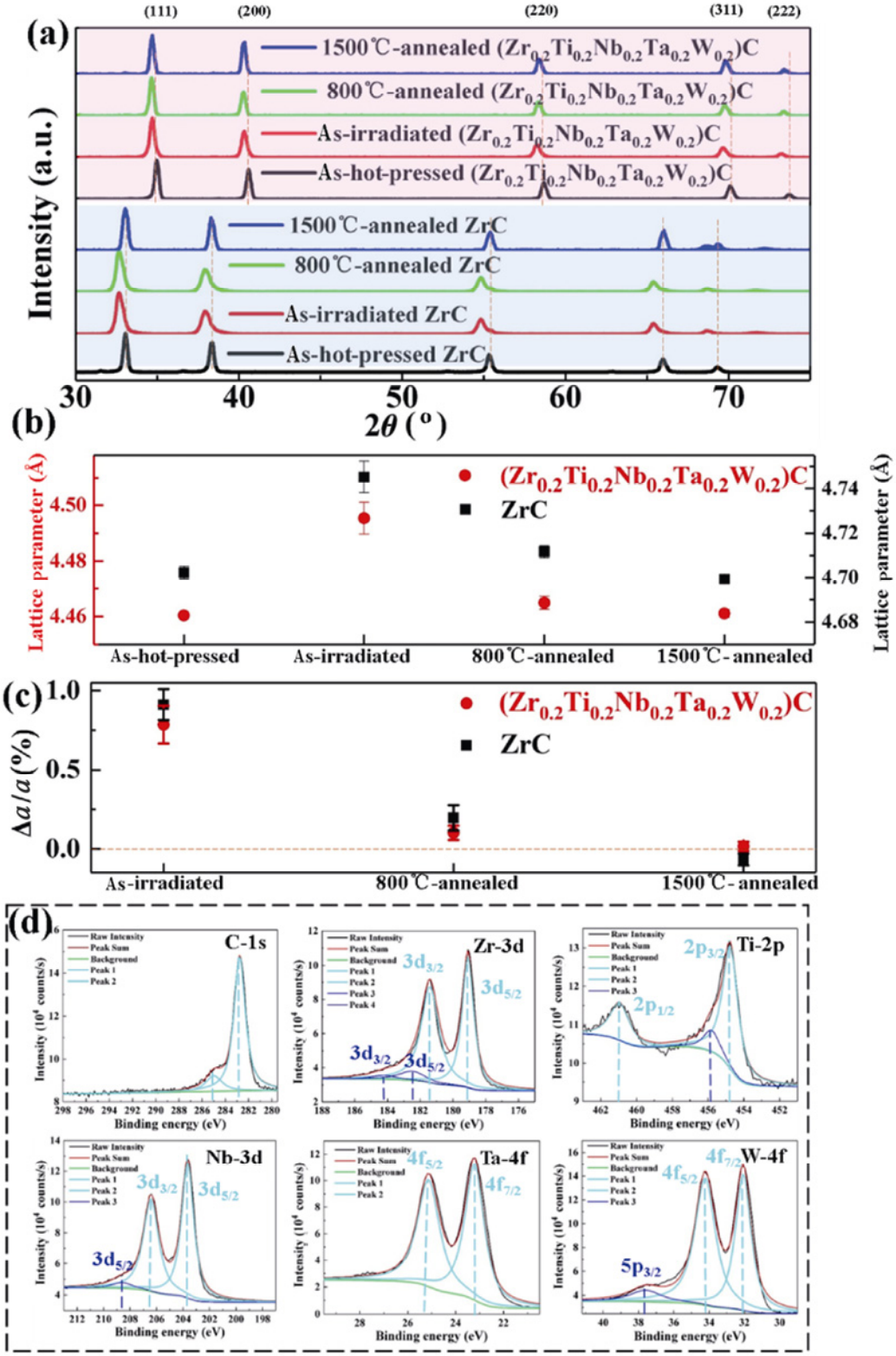

Fig. 2 (a) GIXRD patterns of as-hot-pressed, as-irradiated, and as-annealed ceramics at θ = 3.0° and 4.5° for ZrC and $(Zr_{0.2}Ti_{0.2}Nb_{0.2}Ta_{0.2}W_{0.2})C$, respectively. Changing of (b) a and (c) $\Delta a/a$ for $(Zr_{0.2}Ti_{0.2}Nb_{0.2}Ta_{0.2}W_{0.2})C$ and ZrC during different processes. (d) C 1s, Zr 3d, Ti 2p, Nb 3d, Ta 4f, and W 4f XPS spectra of as-synthesized $(Zr_{0.2}Ti_{0.2}Nb_{0.2}Ta_{0.2}W_{0.2})C$.

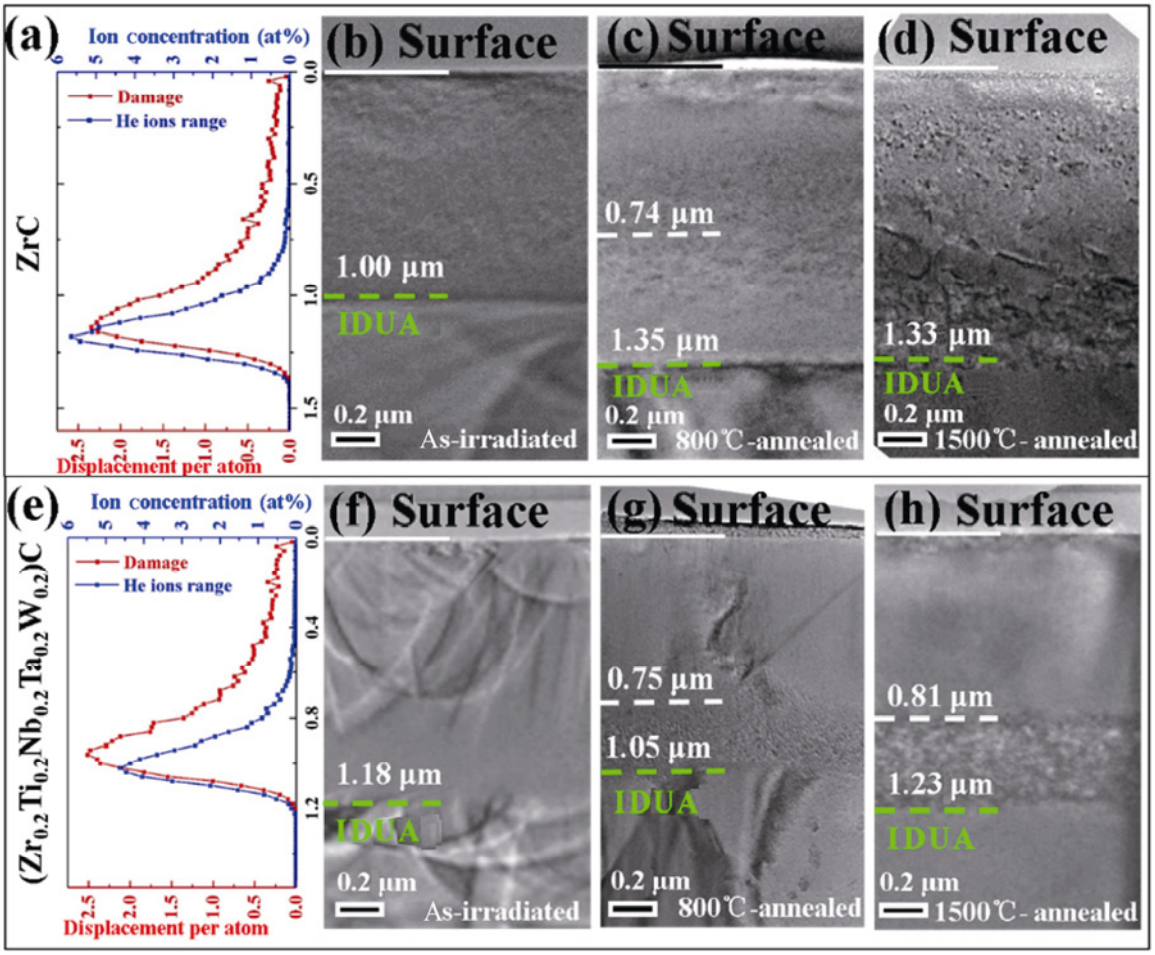

Fig. 3 Damage and He ion ranges of (a) ZrC and (e) $(Zr_{0.2}Ti_{0.2}Nb_{0.2}Ta_{0.2}W_{0.2})C$ calculated by SRIM. Corresponding cross-sectional BF images of as-irradiated (b) ZrC and (f) $(Zr_{0.2}Ti_{0.2}Nb_{0.2}Ta_{0.2}W_{0.2})C$, 800 ℃-annealed (c) ZrC and (g) $(Zr_{0.2}Ti_{0.2}Nb_{0.2}Ta_{0.2}W_{0.2})C$, and 1500 ℃-annealed (d) ZrC and (h) $(Zr_{0.2}Ti_{0.2}Nb_{0.2}Ta_{0.2}W_{0.2})C$.

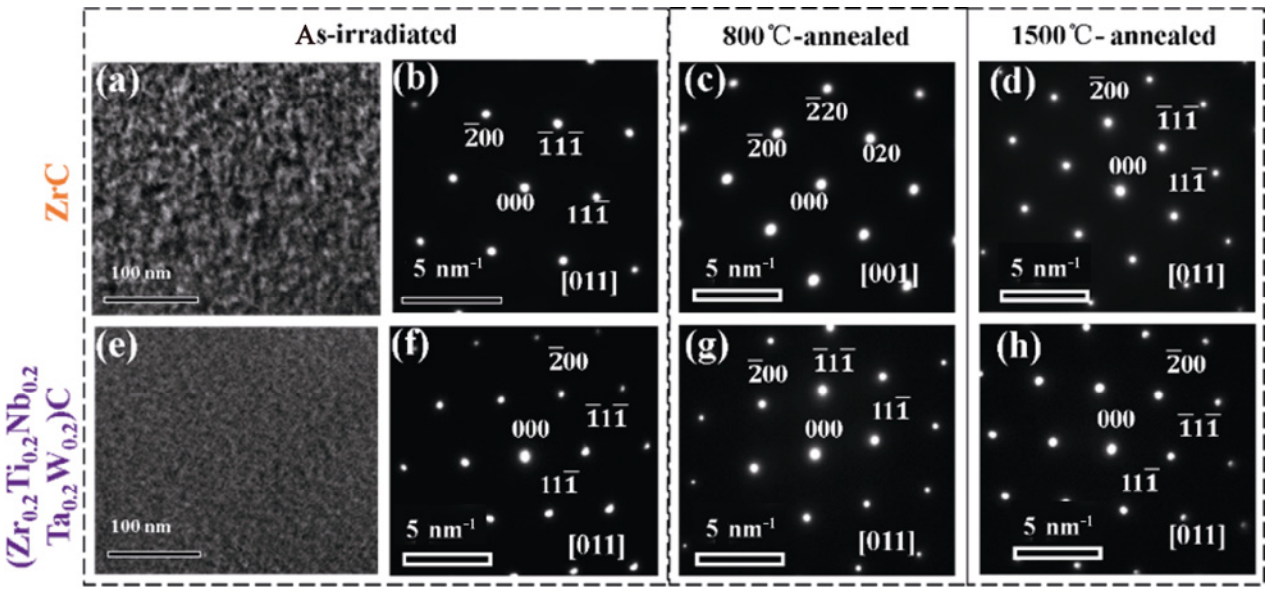

Fig. 4 (a, e) BF images of irradiated area near IDUA and (b, f) corresponding SAED patterns for as-irradiated ZrC and $(Zr_{0.2}Ti_{0.2}Nb_{0.2}Ta_{0.2}W_{0.2})C$. SAED patterns of 800 ℃-annealed (c) ZrC and (g) $(Zr_{0.2}Ti_{0.2}Nb_{0.2}Ta_{0.2}W_{0.2})C$ and 1500 ℃-annealed (d) ZrC, and (h) $(Zr_{0.2}Ti_{0.2}Nb_{0.2}Ta_{0.2}W_{0.2})C$.

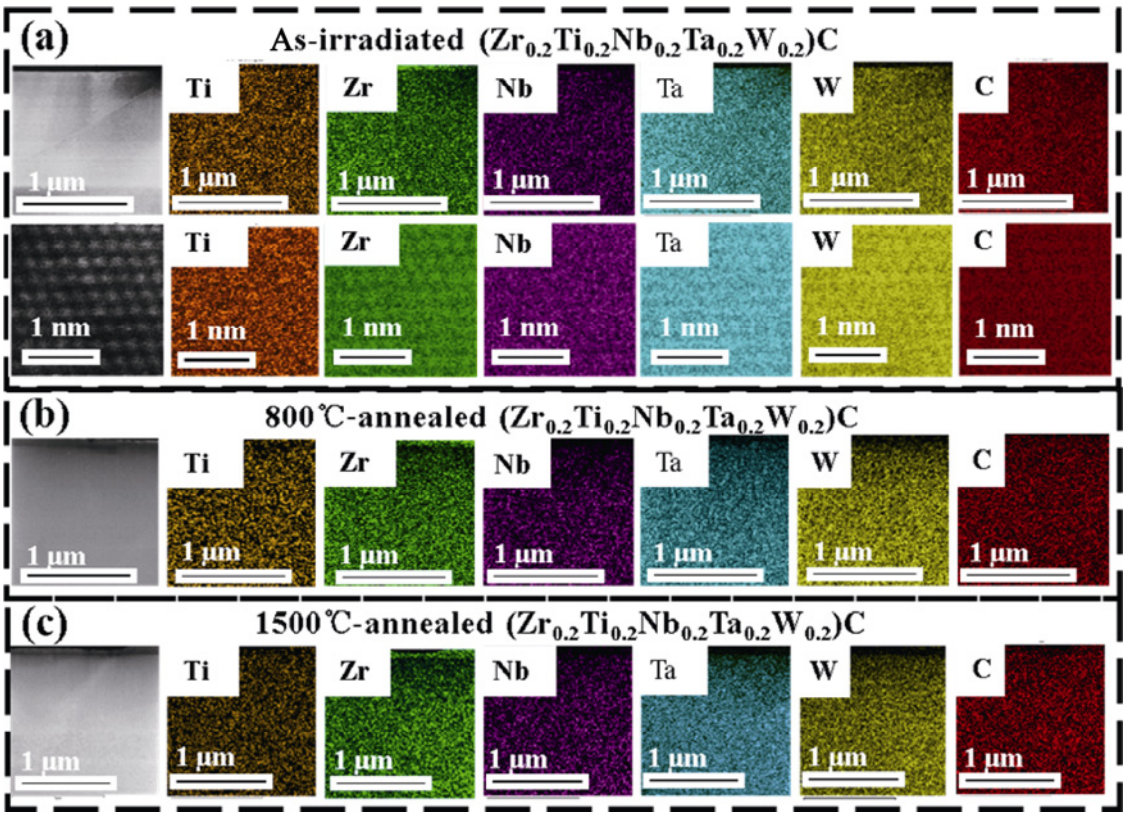

Fig. 5 (a) HAADF image, atomic HAADF image, and corresponding EDS mappings of as-irradiated $(Zr_{0.2}Ti_{0.2}Nb_{0.2}Ta_{0.2}W_{0.2})C$. HAADF image and corresponding EDS mappings of (b) 800 ℃-annealed $(Zr_{0.2}Ti_{0.2}Nb_{0.2}Ta_{0.2}W_{0.2})C$ and (c) 1500 ℃-annealed $(Zr_{0.2}Ti_{0.2}Nb_{0.2}Ta_{0.2}W_{0.2})C$.

Generally, irradiation-induced interstitial defects will result in the lattice expansion and hence large internal strain [46], while the reduction of such lattice strain could be realized via either forming extended defects such as dislocations, suppressing the generation of interstitials or/and interstitial clusters, or sinking interstitials. In Figs. 3(b), 3(f), 4(a), and 4(e), no visible dislocations could be resolved in as-irradiated ZrC and $(Zr_{0.2}Ti_{0.2}Nb_{0.2}Ta_{0.2}W_{0.2})C$. Besides, it can be expected that Ti, Nb, and W atoms would displace more easily than Zr due to their lower bond dissociation energy, as shown in Table 1. Thus, the point defects/atomic displacement should be easier to occur in $(Zr_{0.2}Ti_{0.2}Nb_{0.2}Ta_{0.2}W_{0.2})C$ than in ZrC during irradiation, leading to the observed deeper depth of the IDUA even though $(Zr_{0.2}Ti_{0.2}Nb_{0.2}Ta_{0.2}W_{0.2})C$ has higher mass density than ZrC. However, in the presence of chemical disorder, the longer-time defect evolution rather than the primary damage should play a prominent role in the irradiation behavior [47]. The point defect cluster in the irradiated area of $(Zr_{0.2}Ti_{0.2}Nb_{0.2}Ta_{0.2}W_{0.2})C$ (~3.26 nm) is significantly smaller than that of ZrC (~5.43 nm) (Figs. 4(e) and 4(a), respectively), indicating that the high-entropy structural stabilization effect would enhance the self-repair of the defects, and the sluggish diffusion effect would inhibit the aggregation and growth of the defects [28,48]. In addition, the XPS analyses (Fig. 2(d) and Table 3) reveal that the valence states of Ti and Zr are smaller than 4^+, but those of Nb, Ta, and W are higher than 4^+ in as-synthesized $(Zr_{0.2}Ti_{0.2}Nb_{0.2}Ta_{0.2}W_{0.2})C$, as obtained by referring to the BE of the single carbides. The variations of the valence states for different solute elements arise from their being in different groups, which are then expected to generate anion and/or cation vacancies in the ceramics for charge compensation [49]. The created vacancies are supposed to be able to sink interstitial defects [50]. Besides, the ionization-induced local high temperatures may promote the annihilation of the defects, which could be more prominent in the HECs due to the lattice strain-induced decrease of thermal conductivity. Then, the combination of structural stabilization, sluggish diffusion, valence compensation, and lattice strain aroused in a high-entropy system finally gives rise to the suppression of lattice expansion and smaller point defect clusters and hence higher resistivity to the irradiation damage.

Table 3 BE of XPS peak components of Ar^+ ion etched $(Zr_{0.2}Ti_{0.2}Nb_{0.2}Ta_{0.2}W_{0.2})C$ samples

XPS peak	Experimental BE (eV)	Reference BE (eV)	Reference bond type	Ref.
C 1s	284.8	284.78	Amorphous carbon	[51,52]
C 1s	282.76	282	ZrC	[53]
		281.9	TiC	[54]
		281.63	TiC	[55]
		282.5	NbC	[51]
		282.8	TaC	[56]
		282.28	WC	[52]
Zr $3d_{5/2}$	179.07	179.6	ZrC	[53]
Zr $3d_{3/2}$	181.45	181.6	ZrC	[53]
Zr $3d_{5/2}$	182.5	182.5	ZrO_2	[53]
Zr $3d_{3/2}$	184.2	184.6	ZrO_2	[53]
Ti $2p_{3/2}$	454.8	455	TiC	[54]
Ti $2p_{1/2}$	460.9	461	TiC	[54]
	456.3	456.4	$TiC_{0.81}$	[55]
Nb $3d_{5/2}$	203.65	203.7	NbC (Nb^{3+})	[51]
Nb $3d_{5/2}$	208.6	207.6	NbC (Nb^{4+})	[51]
Nb $3d_{3/2}$	206.42	206.4	NbC (Nb^{3+})	[51]
Ta $4f_{7/2}$	23.21	23.19	TaC	[56]
Ta $4f_{5/2}$	25.13	25.1	TaC	[56]
W $4f_{7/2}$	32.06	31.55	WC (W^{4+})	[52]
W $4f_{5/2}$	34.21	33.66	WC (W^{4+})	[52]
W $5p_{3/2}$	37.6	37.16	WC (W^{6+})	[52]

3.3 Structural and microstructural evolution of as-irradiated $(Zr_{0.2}Ti_{0.2}Nb_{0.2}Ta_{0.2}W_{0.2})C$ and ZrC under annealing

To cope with the future high demands on secure high-temperature response at normal conditions (400–800 ℃) and nuclear accidents (unexpected high temperatures), the as-irradiated ZrC and $(Zr_{0.2}Ti_{0.2}Nb_{0.2}Ta_{0.2}W_{0.2})C$ samples were annealed at 800 and 1500 ℃ to investigate the evolution of irradiated structures. As can be seen from both GIXRD (Fig. 2(a)) and SAED patterns (Fig. 4), the diffraction peaks and spots keep sharp and complete, illustrating that ZrC and $(Zr_{0.2}Ti_{0.2}Nb_{0.2}Ta_{0.2}W_{0.2})C$ maintain lattice integrity after annealing. Figure 2(a) shows that the diffraction peaks shift back close to those of the pristine ceramics. It can be concluded that the heat treatment can eliminate the point defects and recover the parent crystal lattice. The as-irradiated ZrC shows residual 0.20% lattice expansion, while $(Zr_{0.2}Ti_{0.2}Nb_{0.2}Ta_{0.2}W_{0.2})C$ shows only 0.10% after 800 ℃-annealing (Figs. 2(b) and 2(c)). The full recovery could be realized after 1500 ℃-annealing for both ZrC and $(Zr_{0.2}Ti_{0.2}Nb_{0.2}Ta_{0.2}W_{0.2})C$. The cross-sectional microstructures of 800 ℃-annealed ZrC (Fig. 3(c)) and $(Zr_{0.2}Ti_{0.2}Nb_{0.2}Ta_{0.2}W_{0.2})C$ (Fig. 3(g)) show that the depth of the IDUA increases in ZrC (from 1.00 to 1.35 μm) while unexpectedly reducing in $(Zr_{0.2}Ti_{0.2}Nb_{0.2}Ta_{0.2}W_{0.2})C$ (from 1.18 to 1.05 μm). Besides, there appears an additional interface at a lower depth of around 0.75 μm for both ZrC and $(Zr_{0.2}Ti_{0.2}Nb_{0.2}Ta_{0.2}W_{0.2})C$. The brighter contrast in-between the two interfaces in 800 ℃-annealed ZrC (Fig. 3(c)) is mainly caused by the accumulation of the light element He, as we can observe small He bubbles (~2 nm) in this layer (Figs. 6(a) and 6(b)). The He exists in ZrC after irradiation mainly in the forms of He@C and/or He@Zr vacancies and/or He interstitials and concentrates in the comparatively deep region (Fig. 3). Reference [18] discloses that the He atoms tend to be mobile due to low migration barriers. Annealing provides external energy to He for its movement, and thus brings about the formation of the He bubbles, while few He atoms should have been released out of the sample due to very low contents of He near the surface of the irradiated sample. The mottled contrast in-between the two interfaces in 800 ℃-annealed $(Zr_{0.2}Ti_{0.2}Nb_{0.2}Ta_{0.2}W_{0.2})C$ (Fig. 3(g)) is caused by the accumulation of defect clusters, as we can observe dislocations on the nano size along with tiny He bubbles (~1 nm) in this layer (Figs. 6(c) and 6(d)). Thus, the deepening of the IDUA depth in ZrC could be attributed to the diffusion of the He atoms and defects, and their accumulation takes place around the depth region with the peaked residence of the He ions and damage (Figs. 3(a) and 3(e)). It seems that the He atoms and defects are easier to diffuse in ZrC than in $(Zr_{0.2}Ti_{0.2}Nb_{0.2}Ta_{0.2}W_{0.2})C$. The depth of the IDUA in $(Zr_{0.2}Ti_{0.2}Nb_{0.2}Ta_{0.2}W_{0.2})C$ becomes deeper, and the width between the two interfaces increases in the 1500 ℃-annealed samples. However, the position of the IDUA hardly changes in ZrC, but the dislocations with a high density are observed in the whole damaged area, as shown in Fig. 3(d). The dislocations could also be observable in $(Zr_{0.2}Ti_{0.2}Nb_{0.2}Ta_{0.2}W_{0.2})C$ but located only at the depth region of 0.81–1.23 μm (Fig. 3(h)) and appeared shorter and sparser. Thus, the structural evolution during annealing seems to inherit or be restrained by the as-irradiated morphologies. The narrow damaged layer at a certain depth in $(Zr_{0.2}Ti_{0.2}Nb_{0.2}Ta_{0.2}W_{0.2})C$ (Fig. 3(f)) evolved into a He-accumulation layer with

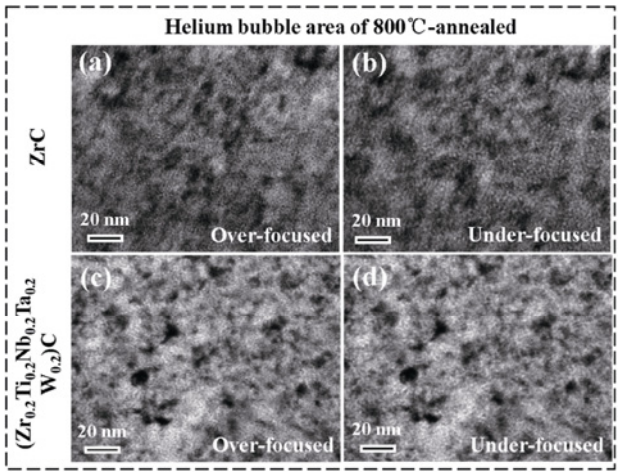

Fig. 6 (a, c) Over-focused and (b, d) under-focused images of He bubble areas in 800 ℃ -annealed (a, b) ZrC and (c, d) $(Zr_{0.2}Ti_{0.2}Nb_{0.2}Ta_{0.2}W_{0.2})C$. He bubbles appear as dark dots in over-focused images and bright dots in under-focused images.

sparse dislocations (Figs. 3(g) and 3(h)), while ZrC was subjected to the damages initiated from the sample surface, which transformed to the dislocations with a high density and the He bubbles in the whole irradiated area after annealing. This further indicates that the sluggish diffusion of the high entropy also restrains the migration of He and defects during annealing. The EDS analysis (Figs. 5(b) and 5(c)) does not observe any elemental segregation in the as-annealed $(Zr_{0.2}Ti_{0.2}Nb_{0.2}Ta_{0.2}W_{0.2})C$.

The ability to suppress the formation of the voids or He bubbles during irradiation is the key requirement for the nuclear materials. The present study indicates the enhanced impediment of the He bubble growth in the high-entropy carbides. As can be seen from Figs. 7(a) and 7(b), it is hard to resolve the He bubbles in the present as-irradiated ZrC and $(Zr_{0.2}Ti_{0.2}Nb_{0.2}Ta_{0.2}W_{0.2})C$, respectively, although tiny He bubbles with a size of ~1 nm are reported in $(Hf_{0.2}Zr_{0.2}Ta_{0.2}Nb_{0.2}Ti_{0.2})C$ after irradiation with 120 keV He ions at room temperature [34]. Actually, Refs. [18,57] could hardly find any He bubbles in as-irradiated ZrC at room temperature either. After annealing at 800 ℃, tiny He bubbles with a size of < 2 nm can be resolved in both ZrC and $(Zr_{0.2}Ti_{0.2}Nb_{0.2}Ta_{0.2}W_{0.2})C$, as marked by the yellow arrows in Figs. 7(c) and 7(d), respectively. Upon increasing the annealing temperature up to 1500 ℃, larger He bubbles are generated, as could be clearly seen in the HAADF images (Figs. 7(e) and 7(f)) and BF images (Fig. 8). The average diameters and density of the He bubbles along the depth were statistically measured, as shown in Figs. 7(g) and 7(h), respectively. For ZrC, the diameter of the He bubbles per fixed depth range (60 nm) reaches the maximum of ~6.18 nm near the IDUA and decreases to ~4.63 nm at a shallow depth of around 1.08 μm, and the mean diameter is 5.52±1.13 nm. Apparently, the abnormal growth of the He bubbles occurs around the IDUA in ZrC. In contrast, the size distribution of the He bubbles in 1500 ℃-annealed $(Zr_{0.2}Ti_{0.2}Nb_{0.2}Ta_{0.2}W_{0.2})C$ is relatively uniform. From the depth of ~0.81 μm to the IDUA, the

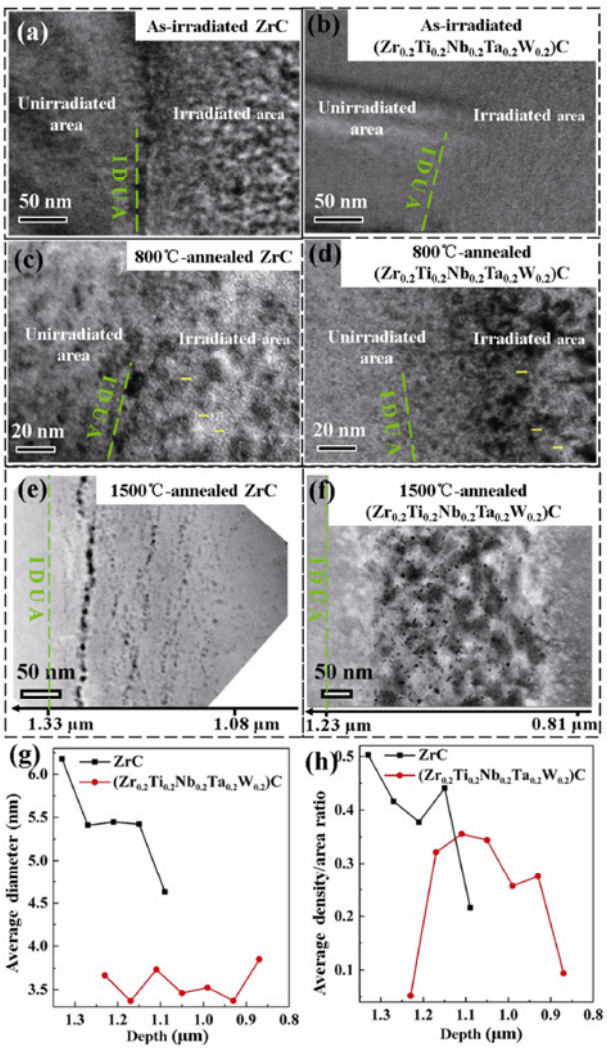

Fig. 7 Under-focused images of as-irradiated (a) ZrC and (b) $(Zr_{0.2}Ti_{0.2}Nb_{0.2}Ta_{0.2}W_{0.2})C$ and 800 ℃-annealed (c) ZrC and (d) $(Zr_{0.2}Ti_{0.2}Nb_{0.2}Ta_{0.2}W_{0.2})C$. HAADF images of 1500 ℃-annealed (e) ZrC and (f) $(Zr_{0.2}Ti_{0.2}Nb_{0.2}Ta_{0.2}W_{0.2})C$. He bubble (g) average diameters and (h) average density/area ratios of 1500 ℃-annealed ZrC and $(Zr_{0.2}Ti_{0.2}Nb_{0.2}Ta_{0.2}W_{0.2})C$ (580 He bubbles were measured in an area of 0.14 μm^2 of 1500 ℃-annealed ZrC, and 1318 bubbles were measured in an area of 0.21 μm^2 of 1500 ℃ -annealed $(Zr_{0.2}Ti_{0.2}Nb_{0.2}Ta_{0.2}W_{0.2})C$. The average density of He bubbles is obtained by calculating their area ratios).

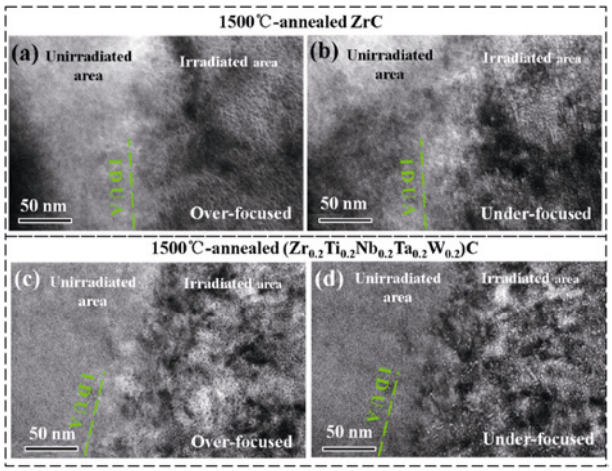

Fig. 8 Cross-sectional BF over-focused and under-focused images of 1500 ℃-annealed (a, b) ZrC and (c, d) $(Zr_{0.2}Ti_{0.2}Nb_{0.2}Ta_{0.2}W_{0.2})C$.

diameter of the He bubbles varies very slightly in the range of ~3.36–3.85 nm, and the mean diameter is 3.51±0.96 nm. The average density/area ratio of the He bubbles is ~40% in 1500 ℃-annealed ZrC. A typical structural feature of the He bubbles in ZrC is that they always align approximately normally to the irradiation direction discretely at different depths. Finally, the abnormally coarsened He bubbles near the IDUA connect to form strings of bubble beads. In contrast, the He bubbles are homogeneously dispersed in 1500 ℃-annealed $(Zr_{0.2}Ti_{0.2}Nb_{0.2}Ta_{0.2}W_{0.2})C$ with a lower average density/area ratio of ~24%. Alignment, coarsening, and connection of the He bubbles to form chains, as observed in ZrC, will be prone to forming cracks, which finally lead to the failure of the ceramics. Such feature is avoided in $(Zr_{0.2}Ti_{0.2}Nb_{0.2}Ta_{0.2}W_{0.2})C$.

The dislocations are another structural defects formed in 1500 ℃-annealed ceramics. They are present everywhere in ZrC and become very long above the first interface (Fig. 3(d) and Fig. S1 in the Electronic Supplementary Material (ESM)). However, the dislocations are shorter and only generate near the IDUA in $(Zr_{0.2}Ti_{0.2}Nb_{0.2}Ta_{0.2}W_{0.2})C$ (Fig. 3(h) and Fig. S1 in the ESM). Table 4 compares the dislocation features in these two ceramics, and Fig. 9(a) illustrates the dislocation morphologies near the IDUA region. The dislocations are formed by 1/2<110> Burgers vectors. Both density and length are smaller in the HECs. According to Ref. [18], there seems to be a strong correlation between the growth of the He bubbles and the dislocations. In fact, the dislocations of the highest density appear within the narrow-depth width near the IDUA where the He bubbles are formed, as illustrated in Figs. 7 and 8, and also schematically presented in Fig. 9(b). Obviously, the point defects and He atoms can migrate to the deeper depth below the IDUA and form the dislocations and He bubbles during annealing at 1500 ℃. The irradiation-induced lattice expansion will create a vertical component of the compressive stress inside the damaged layer, which extends to the undamaged region, and then promotes the migration of point defects to the deeper depth during annealing. The irradiation-induced stress is estimated to be about 4.11 and 4.86 GPa for ZrC and $(Zr_{0.2}Ti_{0.2}Nb_{0.2}Ta_{0.2}W_{0.2})C$, respectively, by Hooke's law, suggesting the elastic modulus of ZrC to be 451.6 GPa and $(Zr_{0.2}Ti_{0.2}Nb_{0.2}Ta_{0.2}W_{0.2})C$ to be 623.5 GPa [58]. COMSOL calculations indicate that the stress is decreased layer by layer along the depth in as- irradiated ZrC (Fig. 9(c)), regardless of a horizontal force. This results in gradient changes in the features of the as-generated He bubbles and dislocations layer by layer along the depth (Fig. 9(b)) during high-temperature annealing to maintain the equilibrium of forces. A representative feature is that the size of the He bubbles varies drastically with depth in 1500 ℃-annealed ZrC (Figs. 7(e), 8(a), and 8(b)). However, it can be seen from Fig. 9(c) and Fig. S2 in the ESM that the severe lattice strain (giving rise to atomic local stress field) in high-entropy $(Zr_{0.2}Ti_{0.2}Nb_{0.2}Ta_{0.2}W_{0.2})C$ owns the ability to the disperse stress, leading to lower lattice expansion after irradiation, more uniform and smaller He bubbles, and shorter and sparser dislocations under annealing at 1500 ℃. Furthermore, the charge compensation-induced vacancies in high-entropy $(Zr_{0.2}Ti_{0.2}Nb_{0.2}Ta_{0.2}W_{0.2})C$ can sink and disperse the He atoms and block the growth of the dislocations, which also play an important role in reducing the irradiation damage.

Table 4 Density and length of dislocations in 1500 ℃-annealed ZrC and 1500 ℃-annealed $(Zr_{0.2}Ti_{0.2}Nb_{0.2}Ta_{0.2}W_{0.2})C$

Material	Depth (μm)	Density of dislocation (10^{-4} nm^{-3})	Length of dislocation (nm)
ZrC [18]	0–0.63	0.757	50–150
	0.63–1.08	0.975	150–400
	1.08–1.31	2.71	28–116
$(Zr_{0.2}Ti_{0.2}Nb_{0.2}Ta_{0.2}W_{0.2})C$	0–0.80	0	0
	0.80–1.23	2.33	25–165

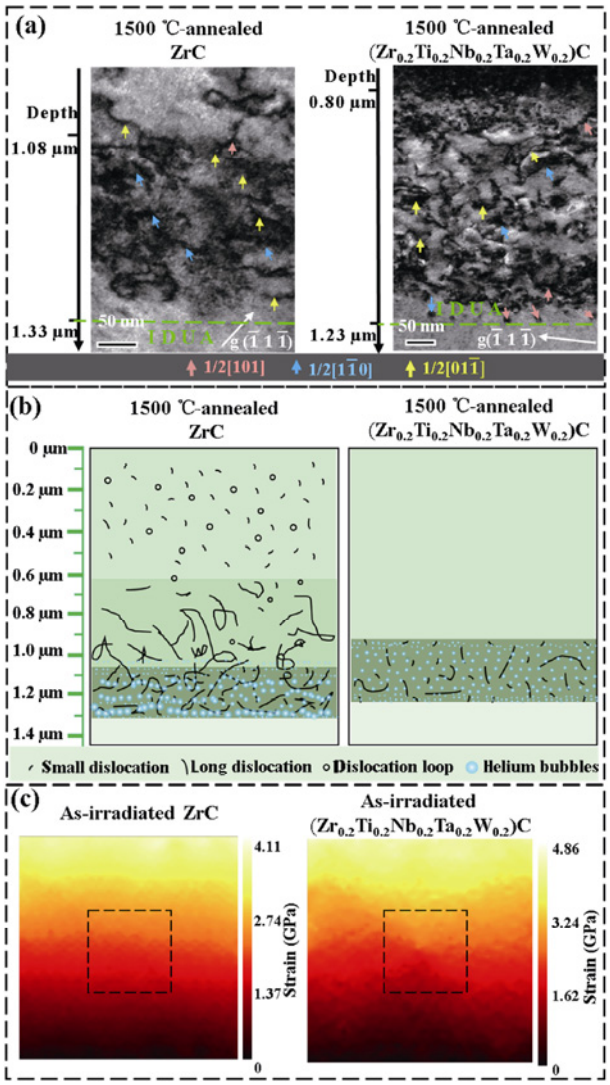

Fig. 9 (a) BF images acquired by ($\bar{1}1\bar{1}$) reflection showing dislocations in 1500 ℃-annealed ZrC and $(Zr_{0.2}Ti_{0.2}Nb_{0.2}Ta_{0.2}W_{0.2})C$. Burgers vectors are marked by different colors. (b) Schematic diagrams presenting morphologies and distributions of dislocations and He bubbles in 1500 ℃-annealed ZrC and $(Zr_{0.2}Ti_{0.2}Nb_{0.2}Ta_{0.2}W_{0.2})C$. (c) Vertical component stress distributions in as-irradiated ZrC and $(Zr_{0.2}Ti_{0.2}Nb_{0.2}Ta_{0.2}W_{0.2})C$, as simulated by COMSOL Multiphysics software.

4 Conclusions

In this study, we investigate the effects of the high entropy on the irradiation behavior of ZrC-based ceramics under 540 keV He ion irradiation with a dose of 1×10^{17} cm^{-2}. Both ZrC and $(Zr_{0.2}Ti_{0.2}Nb_{0.2}Ta_{0.2}W_{0.2})C$ maintain lattice integrity after irradiation at room temperature and also during succeeding annealing processes at high temperatures of 800 and 1500 ℃. However, the irradiation-induced lattice expansion is smaller in $(Zr_{0.2}Ti_{0.2}Nb_{0.2}Ta_{0.2}W_{0.2})C$ (0.78%) than that in ZrC (0.91%) along with smaller point defect clusters formed in the HEC carbides. After annealing at 800 ℃, ZrC exhibits the residual 0.20% lattice expansion, while $(Zr_{0.2}Ti_{0.2}Nb_{0.2}Ta_{0.2}W_{0.2})C$ shows only 0.10%. Both ceramics fully recover their lattices after annealing at 1500 ℃. Tiny He bubbles (~1–2 nm) are generated in both ceramics after annealing at 800 ℃ but migrate back to a shallower depth in $(Zr_{0.2}Ti_{0.2}Nb_{0.2}Ta_{0.2}W_{0.2})C$ contrary to the normal deeper migration, as observed in ZrC. The He bubbles are coarsened, and the dislocations are produced after annealing at 1500 ℃. However, the He bubbles align at a certain depth and gradually grow layer by layer along the depth in ZrC. Finally, the abnormally coarsened bubbles connect and form chains near the damaged–undamaged interface, which apparently implies the risks of cracking and material failure. Such a negative feature is avoided in $(Zr_{0.2}Ti_{0.2}Nb_{0.2}Ta_{0.2}W_{0.2})C$, where the He bubbles have uniform and smaller average sizes and distribute homogeneously. Meanwhile, shorter and sparser dislocations are observed in $(Zr_{0.2}Ti_{0.2}Nb_{0.2}Ta_{0.2}W_{0.2})C$ than those in ZrC. High-entropy-induced higher phase stability and sluggish diffusion of interstitials and He atoms along with the production of vacancies by valence compensation should be responsible for smaller lattice expansion during irradiation and smaller He bubbles and dislocation density during annealing. The theoretical investigation further indicates the dispersion of the internal stress in the as-irradiated HECs, which avoids abnormal growth and adhesion of the He bubbles and dislocations. The present work manifests and quantifies the advantages of the HEC carbides in the irradiation resistance.

Acknowledgements

The present work is financially supported by the National Natural Science Foundation of China (52032001, 52102081, and 51532009), Shanghai Sailing Program (20YF1455500), Science and Technology Commission of Shanghai Municipality (16DZ2260603), and Shanghai Technical Platform for Testing and Characterization on Inorganic Materials (19DZ2290700). The implantation was performed at the 320 kV platform for multi-disciplinary research with highly charged ions at Institute of Modern Physics, Chinese Academy of Sciences.

Electronic Supplementary Material

Supplementary material is available in the online version of this article at https://doi.org/10.26599/JAC.2023.9220727.

References

[1] Zinkle SJ, Was GS. Materials challenges in nuclear energy. *Acta Mater* 2013, **61**: 735–758.

[2] Yvon P, Carré F. Structural materials challenges for advanced reactor systems. *J Nucl Mater* 2009, **385**: 217–222.

[3] Bao WC, Xue JX, Liu JX, *et al*. Coating SiC on zircaloy-4 by magnetron sputtering at room temperature. *J Alloys Compd* 2018, **730**: 81–87.

[4] Gosset D, Dollé M, Simeone D, *et al*. Structural evolution of zirconium carbide under ion irradiation. *J Nucl Mater* 2008, **373**: 123–129.

[5] Keilholtz GW, Moore RE, Osborne MF. Fast-neutron effects on the carbides of titanium, zirconium, tantalum, niobium, and tungsten. *Nucl Technol* 1968, **4**: 330–336.

[6] Ni DW, Cheng Y, Zhang JP, *et al*. Advances in ultra-high temperature ceramics, composites, and coatings. *J Adv Ceram* 2022, **11**: 1–56.

[7] Gu YF, Liu JX, Xu FF, *et al*. Pressureless sintering of titanium carbide doped with boron or boron carbide. *J Eur Ceram Soc* 2017, **37**: 539–547.

[8] Alangi N, Mukherjee J. Liquid gadolinium corrosion study of TaC coating on tantalum. *Ceram Int* 2018, **44**: 19619–19623.

[9] Ozaki Y, Zee RH. Investigation of thermal and hydrogen effects on emissivity of refractory metals and carbides. *Mater Sci Eng* 1995, **202**: 134–141.

[10] Li F, Huang X, Liu JX, *et al*. Sol–gel derived porous ultra-high temperature ceramics. *J Adv Ceram* 2020, **9**: 1–16.

[11] Träskelin P, Björkas C, Juslin N, *et al*. Radiation damage in WC studied with MD simulations. *Nucl Instrum Meth B* 2007, **257**: 614–617.

[12] Reynolds GH, Janvier JC, Kaae JL, *et al*. Irradiation behavior of experimental fuel particles containing chemically vapor deposited zirconium carbide coatings. *J Nucl Mater* 1976, **62**: 9–16.

[13] Snead LL, Katoh Y, Kondo S. Effects of fast neutron irradiation on zirconium carbide. *J Nucl Mater* 2010, **399**: 200–207.

[14] Pierson HO. *Handbook of Refractory Carbides and Nitrides: Properties, Characteristics, Processing and Applications*. New Jersey, USA: Noyes Publications, 1996.

[15] Sevy A, Matthew DJ, Morse MD. Bond dissociation energies of TiC, ZrC, HfC, ThC, NbC, and TaC. *J Chem Phys* 2018, **149**: 044306.

[16] Sabor S, Fadili D, Touimi Benjelloun A, *et al*. Computational spectroscopy of diatomic tungsten carbide, WC. *J Mol Spectrosc* 2020, **371**: 111305.

[17] Murray RL. *Nuclear Energy: An Introduction to the Concepts, Systems, and Applications of Nuclear Processes*, 6th edn. Oxford, UK: Elsevier, 2009.

[18] Bao WC, Wang XG, Lu Y, *et al*. Effect of native carbon vacancies on evolution of defects in ZrC_{1-x} under He ion irradiation and annealing. *J Mater Sci Technol* 2022, **119**: 87–97.

[19] Beyerlein IJ, Caro A, Demkowicz MJ, *et al*. Radiation damage tolerant nanomaterials. *Mater Today* 2013, **16**: 443–449.

[20] Balasubramanian N. High-entropy alloys: An interview with Jien-Wei Yeh. *MRS Bull* 2016, **41**: 905–906.

[21] Zhang YW, Stocks GM, Jin K, *et al*. Influence of chemical disorder on energy dissipation and defect evolution in concentrated solid solution alloys. *Nat Commun* 2015, **6**: 8736.

[22] Lin YP, Yang TF, Lang L, *et al*. Enhanced radiation tolerance of the Ni–Co–Cr–Fe high-entropy alloy as revealed from primary damage. *Acta Mater* 2020, **196**: 133–143.

[23] Lu CY, Yang TN, Jin K, *et al*. Radiation-induced segregation on defect clusters in single-phase concentrated solid-solution alloys. *Acta Mater* 2017, **127**: 98–107.

[24] Schuh B, Mendez-Martin F, Völker B, *et al*. Mechanical properties, microstructure and thermal stability of a nanocrystalline CoCrFeMnNi high-entropy alloy after severe plastic deformation. *Acta Mater* 2015, **96**: 258–268.

[25] Jin K, Lu C, Wang LM, *et al*. Effects of compositional complexity on the ion-irradiation induced swelling and hardening in Ni-containing equiatomic alloys. *Scripta Mater* 2016, **119**: 65–70.

[26] Chen D, Tong Y, Li H, *et al*. Helium accumulation and bubble formation in FeCoNiCr alloy under high fluence He^+ implantation. *J Nucl Mater* 2018, **501**: 208–216.

[27] Chen D, Zhao SJ, Sun JR, *et al*. Diffusion controlled helium bubble formation resistance of FeCoNiCr high-entropy alloy in the half-melting temperature regime. *J Nucl Mater* 2019, **526**: 151747.

[28] Lu CY, Niu LL, Chen NJ, *et al*. Enhancing radiation tolerance by controlling defect mobility and migration pathways in multicomponent single-phase alloys. *Nat Commun* 2016, **7**: 13564.

[29] Do HS, Lee BJ. Origin of radiation resistance in multi-principal element alloys. *Sci Rep* 2018, **8**: 16015.

[30] Xiang HM, Xing Y, Dai FZ, *et al*. High-entropy ceramics: Present status, challenges, and a look forward. *J Adv Ceram* 2021, **10**: 385–441.

[31] Trachenko K. Understanding resistance to amorphization by radiation damage. *J Phys Condens Matter* 2004, **16**: R1491–R1515.

[32] Carey JJ, Nolan M. Non-classical behaviour of higher valence dopants in chromium(III) oxide by a Cr vacancy compensation mechanism. *J Phys Condens Matter* 2017, **29**: 415501.

[33] Wei BX, Wang D, Wang YJ, *et al*. Microstructure evolution in ZrC_x with different stoichiometries irradiated by four MeV Au ions. *Materials* 2019, **12**: 3768.

[34] Wang F, Yan XL, Shao L, *et al*. Irradiation damage behavior in novel high-entropy carbide ceramics. *Transactions Am Nucl Soc* 2019, **120**: 327.
[35] Wang F, Yan XL, Wang TY, *et al*. Irradiation damage in $(Zr_{0.25}Ta_{0.25}Nb_{0.25}Ti_{0.25})C$ high-entropy carbide ceramics. *Acta Mater* 2020, **195**: 739–749.
[36] Zhu YB, Chai JL, Wang ZG, *et al*. Microstructural damage evolution of $(WTiVNbTa)C_5$ high-entropy carbide ceramics induced by self-ions irradiation. *J Eur Ceram Soc* 2022, **42**: 2567–2576.
[37] Ziegler JF, Ziegler MD, Biersack JP. SRIM—The stopping and range of ions in matter (2010). *Nucl Instrum Meth B* 2010, **268**: 1818–1823.
[38] Bao WC, Liu JX, Wang XG, *et al*. Structural evolution in ZrC–SiC composite irradiated by 4 MeV Au ions. *Nucl Instrum Meth B* 2018, **434**: 23–28.
[39] Agarwal S, Koyanagi T, Bhattacharya A, *et al*. Neutron irradiation-induced microstructure damage in ultra-high temperature ceramic TiC. *Acta Mater* 2020, **186**: 1–10.
[40] Das G, Chatterjee DK, Lipsitt HA. Electron irradiation damage in TiC. *J Mater Sci* 1981, **16**: 3283–3291.
[41] Phillipp F, Saile B, Schmid H, *et al*. Energy and orientation dependence of atom displacement in BCC metals studied by high-voltage electron microscopy. *Phys Lett A* 1979, **73**: 123–126.
[42] Gosset D, Morillo J, Allison C, *et al*. Electron irradiation damage in stoichiometric and substoichiometric tantalum carbides TaC_x Part 1: Threshold displacement energies. *Radiat Eff Defect S* 1991, **118**: 207–224.
[43] Björkas C, Vörtler K, Nordlund K. Major elemental asymmetry and recombination effects in irradiated WC. *Phys Rev B* 2006, **74**: 140103.
[44] Bao WC, Robertson S, Liu JX, *et al*. Structural integrity and characteristics at lattice and nanometre levels of ZrN polycrystalline irradiated by 4 MeV Au ions. *J Eur Ceram Soc* 2018, **38**: 4373–4383.
[45] Bao WC, Robertson S, Zhao JW, *et al*. Structural integrity and damage of ZrB_2 ceramics after 4 MeV Au ions irradiation. *J Mater Sci Technol* 2021, **72**: 223–230.
[46] Yang TF, Taylor CA, Kong SY, *et al*. The discrepancies in multistep damage evolution of yttria-stabilized zirconia irradiated with different ions. *J Nucl Mater* 2013, **443**: 40–48.
[47] Deluigi OR, Pasianot RC, Valencia FJ, *et al*. Simulations of primary damage in a high entropy alloy: Probing enhanced radiation resistance. *Acta Mater* 2021, **213**: 116951.
[48] Harrison RW, Greaves G, Le H, *et al*. Chemical effects on He bubble superlattice formation in high entropy alloys. *Curr Opin Solid St M* 2019, **23**: 100762.
[49] Wright AJ, Wang QY, Huang CY, *et al*. From high-entropy ceramics to compositionally-complex ceramics: A case study of fluorite oxides. *J Eur Ceram Soc* 2020, **40**: 2120–2129.
[50] Xue JX, Zhang GJ, Guo LP, *et al*. Improved radiation damage tolerance of titanium nitride ceramics by introduction of vacancy defects. *J Eur Ceram Soc* 2014, **34**: 633–639.
[51] Gupta A, Pandey OP. Visible irradiation induced photodegradation by NbC/C nanocomposite derived from smoked cigarette litter (filters). *Sol Energy* 2018, **163**: 167–176.
[52] Chen LY, Yi DQ, Wang B, *et al*. Mechanism of the early stages of oxidation of WC–Co cemented carbides. *Corros Sci* 2016, **103**: 75–87.
[53] Balaceanu M, Braic M, Braic V, *et al*. Surface chemistry of plasma deposited ZrC hard coatings. *J Optoelectron Adv M*, 2005, **7**: 2557–2560.
[54] Choi Y, Umebayashi T, Yamamoto S, *et al*. Fabrication of TiO_2 photocatalysts by oxidative annealing of TiC. *J Mater Sci Lett* 2003, **22**: 1209–1211.
[55] Li G, Xia LF. Structural characterization of TiC_x films prepared by plasma based ion implantation. *Thin Solid Films* 2001, **396**: 16–22.
[56] Vargas M, Castillo HA, Restrepo-Parra E, *et al*. Stoichiometry behavior of TaN, TaCN and TaC thin films produced by magnetron sputtering. *Appl Surf Sci* 2013, **279**: 7–12.
[57] Agarwal S, Bhattacharya A, Trocellier P, *et al*. Helium induced microstructure damage, nano-scale grain formation and helium retention behaviour of ZrC. *Acta Mater* 2019, **163**: 14–27.
[58] Guo XJ, Xin XT, Bao WC, *et al*. High hardness (TiZr)C ceramic with dislocation networks. *J Am Ceram Soc* 2022, **105**: 5984–5993.